Aerospace Science and Technology 126 (2022) 107631

Contents lists available at ScienceDirect

Aerospace Science and Technology

www.elsevier.com/locate/aescte

Enhancing navigation integrity for Urban Air Mobility with redundant inertial sensors

Shizhuang Wang [a], Xingqun Zhan [a,*], Yawei Zhai [a], Lingxiao Zheng [a], Baoyu Liu [b]

[a] School of Aeronautics and Astronautics, Shanghai Jiao Tong University, Shanghai, China
[b] Schulich School of Engineering, University of Calgary, Calgary, Canada

ARTICLE INFO

Article history:
Received 11 March 2022
Received in revised form 21 April 2022
Accepted 9 May 2022
Available online 11 May 2022
Communicated by Chaoyong Li

Keywords:
Urban Air Mobility
Integrity
Fault detection
Protection level
Multiple inertial measurement units

ABSTRACT

Urban Air Mobility (UAM) uses highly automated air vehicles to offer safe and efficient low-altitude urban air transportation services, for which ensuring navigation safety (measured by integrity) is an essential precondition. UAM vehicles can navigate themselves using Global Navigation Satellite Systems (GNSS)/Inertial Measurement Unit (IMU) tightly coupled systems. However, these systems are vulnerable to IMU failures aside from GNSS faults, given that UAM vehicles will use low-cost IMUs. IMU faults can severely degrade navigation integrity, thereby threatening UAM operational safety and increasing the difficulty of urban air traffic management. This issue can be mitigated by employing redundant IMUs. Civil aircraft use consistency checks among multiple high-performance Inertial Navigation Systems (INSs) to enhance navigation integrity. But this approach is not suitable for low-cost IMUs because of fast error accumulation. In response, this work proposes a new approach to enhance navigation integrity for UAM by integrating multiple IMUs with GNSS. In this approach, multiple IMUs and GNSS are tightly coupled by a centralized Kalman filter, and the corresponding integrity monitoring algorithm is developed to (a) detect the faults in GNSS and/or IMUs and (b) evaluate the probabilistic upper bounds on navigation errors, namely protection levels. Simulations are conducted to demonstrate the proposed method and to present sensitivity analyses, and the results suggest the effectiveness of the new approach. This method is beneficial to improving UAM operational safety and can potentially be applied to civil aircraft in the future.

© 2022 Elsevier Masson SAS. All rights reserved.

1. Introduction

Urban Air Mobility (UAM) envisions a safe and efficient short-range air transportation system that will use highly automated aircraft to transport passengers or cargo at lower altitudes within urban areas [1][2]. UAM has attracted wide interest because it is expected to greatly improve travel efficiency. Operational safety is the paramount aspect of UAM, for which ensuring navigation safety is an essential precondition [3]. Failure to correctly perform the navigation task could potentially lead to catastrophic accidents such as crashes and collisions.

Navigation safety is quantified by integrity in the civil aviation field. Integrity measures the trust that can be placed on the correctness of the navigation output, and it includes the ability to timely inform the users when system anomalies result in unacceptable navigation errors [4]. Because integrity is intended for safety-critical applications, it takes rare events such as measurement faults into account.

Integrity is usually evaluated using integrity monitoring techniques, which simultaneously perform Fault Detection (FD) checks and evaluate the associated Protection Levels (PLs) [5]. The PL is a probabilistic error bound computed to guarantee that the probability of the absolute position error exceeding the said number is smaller than the allowable integrity risk [6]. Fig. 1 explains the meanings of the Horizontal PL (HPL) and the Vertical PL (VPL) in the UAM context.

Global Navigation Satellite Systems (GNSS) have been one of the most important navigation techniques for decades [7]. Recently, civil aircraft also depend more and more on GNSS, and various GNSS integrity monitoring approaches have been developed. The most representative ones are Receiver Autonomous Integrity Monitoring (RAIM) [8] and Advanced RAIM (ARAIM) [9–12]. These methods were originally developed for Least Squares (LS)-based GNSS-standalone systems and were typically implemented in a snapshot way.

Compared to civil aircraft, UAM vehicles will have more stringent performance requirements on onboard navigation systems,

* Corresponding author.
E-mail address: xqzhan@sjtu.edu.cn (X. Zhan).

https://doi.org/10.1016/j.ast.2022.107631
1270-9638/© 2022 Elsevier Masson SAS. All rights reserved.

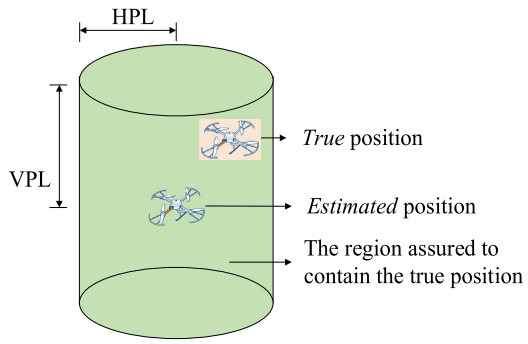

Fig. 1. Illustration of the definition of HPL and VPL in the UAM context.

because (a) they may rely on fewer ground infrastructures, (b) the take-off and landing conditions will be poorer, and (c) the airspace density will be higher. Meanwhile, they will use low-cost sensors for reducing hardware costs. Therefore, using GNSS-standalone systems is no longer feasible, and integrating GNSS with an Inertial Measurement Unit (IMU) will be a satisfactory solution. The integration of GNSS and IMU can be implemented with loose, tight, and deep integration [13] architectures, among which the tight integration architecture is the most suitable for UAM because it achieves a balance between navigation performance and algorithm complexity [14][15].

Evaluating the integrity of GNSS/IMU tightly coupled systems is the premise of applying them to UAM tasks. The tight integration of GNSS and IMU is usually implemented with a Kalman Filter (KF). Different from the snapshot LS, the KF is a time-sequential estimator, i.e., the current estimate is influenced by both current and past measurements. Therefore, the snapshot RAIM and ARAIM methods cannot be directly used to evaluate the integrity of KF-based GNSS/IMU tightly integrated systems.

Recently, various approaches have been developed to improve the robustness of GNSS/IMU tightly coupled systems through Fault Detection and Exclusion (FDE) [16–20]. These approaches were usually implemented based on hypothesis tests, robust estimation, or machine learning. However, they do not evaluate the corresponding integrity risk or PLs, and thus they are not a complete integrity monitoring algorithm.

There have been only a few methods that simultaneously perform the FD checks and evaluate the PLs for GNSS/IMU tightly coupled systems. They usually construct the FD test statistics based on innovation or residual sequences [21–24] rather than snapshot innovation or residual vectors. This is because using snapshot residual or innovation vectors makes it difficult to (a) detect slowly growing errors and (b) evaluate the integrity risk coming from previously undetected faults. Although the methods based on innovation or residual sequences can overcome this shortcoming, they are computationally expensive due to the search for the worst-case fault profile [21,24].

To address these issues, the most recent studies investigated the Multiple Hypothesis Solution Separation (MHSS)-based integrity monitoring methods. MHSS was originally used in the baseline ARAIM algorithm and showed promising performance [9][25]. Based on the equivalence between the KF and a batch LS, MHSS has been successfully applied to perform integrity monitoring of KF-based navigation systems [26–29]. These studies suggest that MHSS-based approaches can produce superior performance to innovation- or residual-based methods [26][27]. Besides, MHSS has two advantages over traditional methods: first, it can naturally accommodate multi-fault cases; second, it provides a straightforward method to evaluate the PLs.

However, most MHSS-based integrity monitoring approaches for GNSS/IMU tightly coupled systems only accounted for GNSS faults. But historical accidents such as the crashes of Qantas F72 have shown the potential safety risk due to IMU failures [30]. This is especially true given that UAM vehicles may be equipped with low-cost IMUs rather than high-performance Inertial Navigation Systems (INSs). The Mean Time Between Failures (MTBF) of some well-known tactical-grade IMUs, such as STIM 210 and HG 4930, is usually about $10^3 \sim 10^5$ hours, and thus the fault probability is $10^{-3} \sim 10^{-5}$ per hour [31,32]. This number is generally much higher than the allowable integrity risk in safety-critical applications. Although a few integrity monitoring approaches have considered the occurrence of IMU failures, they either lacked the rigorous derivations for the PL evaluation or were developed based on snapshot innovations [33,34].

For a GNSS/IMU tightly coupled system, its integrity performance will be severally degraded if the prior probability of IMU failures cannot be ignored. Compared to GNSS satellite faults, IMU failures can exert a more significant effect on navigation integrity. This is because there is only one IMU in the system, and its failure will directly make the system degraded to a GNSS-standalone system. In contrast, if one satellite is faulted, there are still many other satellites that can be used. Therefore, employing redundant IMUs to enhance navigation integrity has become a solid demand for UAM vehicles.

Generally, civil aircraft are equipped with multiple independent high-performance INSs to achieve hardware redundancy, and they perform consistency checks among multiple INSs for improving navigation integrity. However, this approach is not a satisfactory solution for UAM vehicles because they will employ low-cost IMUs and cannot navigate themselves using an INS-standalone system. In response, this work proposes a new approach to enhance navigation integrity for UAM through tightly integrating multiple IMUs with GNSS. The contributions of this work are two folds. First, a centralized Kalman filter framework is established to jointly fuse the measurements from all IMUs and the GNSS receiver. More importantly, an integrity monitoring algorithm for this integrated navigation system is developed to (a) simultaneously detect the faults in IMUs and GNSS satellites and (b) rigorously evaluate the corresponding PLs. In the proposed approach, both information fusion and integrity monitoring are implemented in a centralized way, and thus it can fully exploit the effective information provided by all sensors and is expected to offer satisfactory navigation performance.

The rest of this paper is organized as follows. Section 2 presents the filter design for the tight integration of GNSS and multiple IMUs. Then the corresponding integrity monitoring scheme is developed in Section 3. Multiple sets of simulations are carried out in Section 4 to evaluate the performance of the new method. And finally, Section 5 draws the conclusions.

2. Kalman filter-based tight integration of GNSS and multiple IMUs

In this section, we first briefly present the basic principles of the standard GNSS/IMU tight integration architecture. Based on this, a centralized Kalman filter framework is designed to fuse the measurements from all IMUs and the GNSS receiver. Finally, the advantages of the proposed information fusion strategy over other schemes are discussed.

2.1. Preliminaries on GNSS/IMU tight integration

The tight integration of GNSS and an IMU is usually implemented based on an Error-State Kalman Filter (ESKF) to mitigate the effect of linearization errors [15]. The error state vector is composed of the INS error states and the GNSS receiver clock states, as given below [35]:

$$\mathbf{x} = \left[{}^{\mathrm{I}}\mathbf{x}; {}^{\mathrm{G}}\mathbf{x} \right] \tag{1}$$

with

$${}^{\mathrm{I}}\mathbf{x} = \left[\delta\mathbf{p}; \delta\mathbf{v}; \delta\boldsymbol{\phi}; \nabla_{\mathrm{a}}; \nabla_{\mathrm{g}} \right] \tag{2}$$

$${}^{\mathrm{G}}\mathbf{x} = \left[\delta t_{\mathrm{clk}}; \delta t_{\mathrm{dft}}; \delta t_{\mathrm{sys},2}; \cdots; \delta t_{\mathrm{sys},nc} \right] \tag{3}$$

where $\delta\mathbf{p}$, $\delta\mathbf{v}$, $\delta\boldsymbol{\phi}$ denote the INS position, velocity, and attitude errors in the East-North-Up (ENU) frame; ∇_{a} and ∇_{g} are the accelerometer and gyroscope biases; δt_{clk} and δt_{dft} represent the receiver clock bias and drift; nc is the number of used constellations; $\delta t_{\mathrm{sys},i}$ (i=2, …, nc) denotes the inter-system bias between the i^{th} constellation and the first constellation.

The state propagation model is written as [35]:

$$\mathbf{x}_k = \begin{bmatrix} {}^{\mathrm{I}}\mathbf{F}_k & \\ & {}^{\mathrm{G}}\mathbf{F}_k \end{bmatrix} \mathbf{x}_{k-1} + \begin{bmatrix} {}^{\mathrm{I}}\boldsymbol{\omega}_k \\ {}^{\mathrm{G}}\boldsymbol{\omega}_k \end{bmatrix} \triangleq \mathbf{F}_k \mathbf{x}_{k-1} + \boldsymbol{\omega}_k \tag{4}$$

where $\mathbf{F}_k$ denotes the state transition matrix from epoch $(k-1)$ to epoch k. $\boldsymbol{\omega}_k$ is the process noise vector whose covariance matrix is given by [35]:

$$\mathbf{Q}_k = \begin{bmatrix} {}^{\mathrm{I}}\mathbf{Q}_k & \\ & {}^{\mathrm{G}}\mathbf{Q}_k \end{bmatrix} \tag{5}$$

The measurement model for GNSS pseudoranges is formulated by [35]:

$${}^{\mathrm{G}}\mathbf{z}_k = \begin{bmatrix} {}^{\mathrm{G}}_{\mathrm{I}}\mathbf{H}_k & {}^{\mathrm{G}}_{\mathrm{G}}\mathbf{H}_k \end{bmatrix} \begin{bmatrix} {}^{\mathrm{I}}\mathbf{x} \\ {}^{\mathrm{G}}\mathbf{x} \end{bmatrix} + {}^{\mathrm{G}}\boldsymbol{\upsilon}_k \triangleq {}^{\mathrm{G}}\mathbf{H}_k \mathbf{x}_k + {}^{\mathrm{G}}\boldsymbol{\upsilon}_k \tag{6}$$

where ${}^{\mathrm{G}}\mathbf{z}_k$ equals to the pseudorange vector minus the equivalent pseudorange vector derived from the INS solution. As $\mathbf{x}$ consists of ${}^{\mathrm{I}}\mathbf{x}$ and ${}^{\mathrm{G}}\mathbf{x}$, the measurement matrix ${}^{\mathrm{G}}\mathbf{H}_k$ is composed of ${}^{\mathrm{G}}_{\mathrm{I}}\mathbf{H}_k$ and ${}^{\mathrm{G}}_{\mathrm{G}}\mathbf{H}_k$ accordingly. ${}^{\mathrm{G}}\boldsymbol{\upsilon}_k$ is the measurement noise vector, and its covariance matrix is ${}^{\mathrm{G}}\mathbf{R}_k$. The detailed expressions of the models above can be found in [35].

Based on the models above, the state vector can be estimated using a KF. The KF includes two steps: prediction and update. The prediction step is to propagate the states and their covariance as follows:

$$\overline{\mathbf{x}}_k = \mathbf{F}_k \hat{\mathbf{x}}_{k-1} \tag{7}$$

$$\overline{\mathbf{P}}_k = \mathbf{F}_k \hat{\mathbf{P}}_{k-1} \mathbf{F}_k^{\mathrm{T}} + \mathbf{Q}_k \tag{8}$$

where $\mathbf{P}$ is the state error covariance; the symbols "$\bar{}$" and "$\hat{}$" indicate the predicted and updated estimates, respectively.

In the update phase, the estimates are updated by incorporating the new measurements:

$$\mathbf{K}_k = \overline{\mathbf{P}}_k \mathbf{H}_k^{\mathrm{T}} \left(\mathbf{H}_k \overline{\mathbf{P}}_k \mathbf{H}_k^{\mathrm{T}} + \mathbf{R}_k \right)^{-1} \tag{9}$$

$$\hat{\mathbf{x}}_k = \overline{\mathbf{x}}_k + \mathbf{K}_k \left(\mathbf{z}_k - \mathbf{H}_k \overline{\mathbf{x}}_k \right) \tag{10}$$

$$\hat{\mathbf{P}}_k = \left(\mathbf{I} - \mathbf{K}_k \mathbf{H}_k \right) \overline{\mathbf{P}}_k \tag{11}$$

where $\mathbf{K}$ is the Kalman gain. Please note that the left superscript "G" is omitted in these equations.

2.2. Tight integration of GNSS and multiple IMUs based on a centralized Kalman filter

Inspired by the approach in [36], we develop a centralized KF framework to integrate GNSS with a Multi-IMU (MIMU) system. This framework can apply to the MIMU systems with multiple identical or different IMUs. Fig. 2 shows an example of a MIMU system with three IMUs. In this work, it is assumed that (a) all IMUs are rigidly mounted, (b) the extrinsic parameters between every two IMUs are accurately known, and (c) the noises of each IMU are collectively independent.

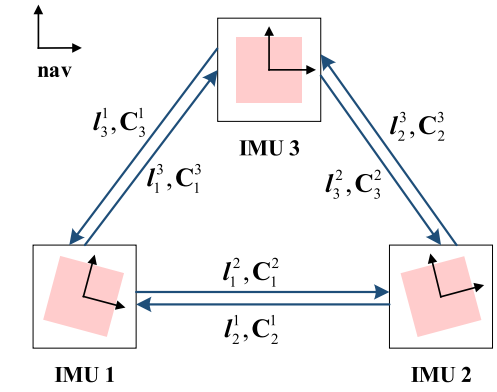

Fig. 2. Two-dimensional illustration of a MIMU system with three IMUs.

In the centralized KF, the state vector is constructed by stacking the state vectors of all IMUs and the GNSS receiver:

$$\mathbf{x} = \left[{}^{\mathrm{I}}_{1}\mathbf{x}; \ldots; {}^{\mathrm{I}}_{m}\mathbf{x}; {}^{\mathrm{G}}\mathbf{x} \right] \tag{12}$$

where the left subscript indicates the IMU index and m is the number of IMUs. Accordingly, the state transition matrix, the process noise vector, and the process noise covariance are respectively given by:

$$\begin{aligned} \mathbf{F}_k &= \begin{bmatrix} {}^{\mathrm{I}}_{1}\mathbf{F}_k & & & \\ & \ddots & & \\ & & {}^{\mathrm{I}}_{m}\mathbf{F}_k & \\ & & & {}^{\mathrm{G}}\mathbf{F}_k \end{bmatrix}, \boldsymbol{\omega}_k = \begin{bmatrix} {}^{\mathrm{I}}_{1}\boldsymbol{\omega}_k \\ \ddots \\ {}^{\mathrm{I}}_{m}\boldsymbol{\omega}_k \\ {}^{\mathrm{G}}\boldsymbol{\omega}_k \end{bmatrix}, \\ \mathbf{Q}_k &= \begin{bmatrix} {}^{\mathrm{I}}_{1}\mathbf{Q}_k & & & \\ & \ddots & & \\ & & {}^{\mathrm{I}}_{m}\mathbf{Q}_k & \\ & & & {}^{\mathrm{G}}\mathbf{Q}_k \end{bmatrix} \end{aligned} \tag{13}$$

Therefore, for a GNSS/MIMU tightly coupled system, the state prediction step can be implemented by substituting (12) and (13) into (7) and (8).

Then, the accurately-known relative poses among different IMUs (i.e., the extrinsic parameters) are used as additional measurements during the filter update stage. The relative pose information describes the relative position and attitude between every two IMUs. Virtual measurements are constructed based on these parameters, and the corresponding measurement models are presented as follows.

For two arbitrary IMUs, i and j, their true attitudes and positions must be consistent with the known relative pose information. Mathematically, the relative-attitude constraint and the relative-position constraint are respectively given by:

$$\mathbf{C}_i^n \left(\mathbf{C}_j^n \mathbf{C}_i^j \right)^{-1} = \mathbf{I} \tag{14}$$

$${}^{\mathrm{I}}_{i}\mathbf{p} - \left({}^{\mathrm{I}}_{j}\mathbf{p} + \mathbf{C}_i^n \boldsymbol{l}_i^j \right) = \mathbf{0} \tag{15}$$

where the superscript n indicates the true navigation frame; $\mathbf{C}_*^n$ ($*=i$ or j) is the transformation matrix from the body frame of

IMU $*$ to the true navigation frame; ${}^{\mathrm{I}}_{*}\mathbf{p}$ denotes the true position of IMU $*$. Because the relative-pose constraints are accurately known, we have the following noise-free measurement equation:

$$\begin{bmatrix} {}^{\mathrm{I}}_{i}\overline{\mathbf{p}} - {}^{\mathrm{I}}_{j}\overline{\mathbf{p}} \\ {}^{i}_{j}\overline{\boldsymbol{\varphi}} \end{bmatrix} = \begin{bmatrix} {}^{i}_{j}\mathbf{H}(1) & \cdots & {}^{i}_{j}\mathbf{H}(m) & \mathbf{0} \end{bmatrix} \cdot \mathbf{x} + \mathbf{0}$$
$$\Longleftrightarrow {}^{i}_{j}\mathbf{z} = {}^{i}_{j}\mathbf{H} \cdot \mathbf{x} + \mathbf{0} \tag{16}$$

where ${}^{i}_{j}\overline{\boldsymbol{\varphi}}$ is a vector defined to quantify the difference between the navigation frame predicted by IMU i and that given by IMU j. Specifically, this vector is determined by:

$$\mathbf{I} - \left({}^{i}_{j}\overline{\boldsymbol{\varphi}}\right)^{\times} \approx \mathbf{C}^{\overline{n}_i}_{\overline{n}_j} = \mathbf{C}^{\overline{n}_i}_{i}\mathbf{C}^{i}_{j}\mathbf{C}^{j}_{\overline{n}_j} \tag{17}$$

where $(\blacksquare)^{\times}$ forms a skew-symmetric matrix about the vector $\blacksquare$; $\overline{n}_i$ and $\overline{n}_j$ are the navigation frames predicted by IMU i and IMU j, respectively.

As shown in (16), the measurement matrix ${}^{i}_{j}\mathbf{H}$ for the virtual measurements is composed of $m+1$ blocks. The last block is associated with the GNSS states, and thus its elements are all zero. And the i^{th} $(1 \le i \le m)$ block corresponds to the states about IMU i, which is a 6×15 matrix given by:

$${}^{i}_{j}\mathbf{H}(o) = \begin{cases} \begin{bmatrix} \mathbf{I} & \mathbf{0} & \mathbf{0} & \mathbf{0} & \mathbf{0} \\ \left(\mathbf{C}^{\hat{n}_i}_{i}\boldsymbol{l}^{j}_{i}\right)\times & \mathbf{0} & \mathbf{I} & \mathbf{0} & \mathbf{0} \end{bmatrix}, & o = i \\ \begin{bmatrix} -\mathbf{I} & \mathbf{0} & \mathbf{0} & \mathbf{0} & \mathbf{0} \\ \mathbf{0} & \mathbf{0} & -\mathbf{I} & \mathbf{0} & \mathbf{0} \end{bmatrix}, & o = j \\ \begin{bmatrix} \mathbf{0} & \mathbf{0} & \mathbf{0} & \mathbf{0} & \mathbf{0} \\ \mathbf{0} & \mathbf{0} & \mathbf{0} & \mathbf{0} & \mathbf{0} \end{bmatrix}, & \text{otherwise} \end{cases} \tag{18}$$

Appendix A provides the detailed derivations for Equations (16)–(18).

For a GNSS/MIMU integrated navigation system, there will be multiple measurement equations derived from the MIMU relative-pose constraints. This work provides two different ways to construct the corresponding measurement models, and their difference mainly lies in whether an IMU is selected as the base.

2.2.1. No-base form

Fig. 3 shows the GNSS/MIMU integration architecture in the no-base form. In this form, the relative pose information between every two IMUs is used to construct the measurement equations, i.e., (16). Besides, GNSS measurements are also cloned to m groups, each of which corresponds to an IMU. Accordingly, the measurement model in this form is given by:

$$\begin{bmatrix} {}^{1}_{2}\mathbf{z}_k \\ \vdots \\ {}^{m}_{m-1}\mathbf{z}_k \\ {}^{\mathrm{G}}_{1}\mathbf{z}_k \\ \vdots \\ {}^{\mathrm{G}}_{m}\mathbf{z}_k \end{bmatrix} = \begin{bmatrix} {}^{1}_{2}\mathbf{H}_k \\ \vdots \\ {}^{m}_{m-1}\mathbf{H}_k \\ {}^{\mathrm{G}}_{1}\mathbf{H}_k \\ \vdots \\ {}^{\mathrm{G}}_{m}\mathbf{H}_k \end{bmatrix} \mathbf{x}_k + \begin{bmatrix} \mathbf{0} \\ \vdots \\ \mathbf{0} \\ {}^{\mathrm{G}}\boldsymbol{\upsilon}_k \\ \vdots \\ {}^{\mathrm{G}}\boldsymbol{\upsilon}_k \end{bmatrix} \Longleftrightarrow \mathbf{z}_k = \mathbf{H}_k\mathbf{x}_k + \boldsymbol{\upsilon}_k \tag{19}$$

where ${}^{\mathrm{G}}_{i}\mathbf{z}_k$ is the cloned GNSS measurement vector for IMU i. It is noteworthy that the cloned GNSS measurements are exactly the same as the original ones.

The measurement matrix ${}^{\mathrm{G}}_{i}\mathbf{H}_k$ is expressed as:

$${}^{\mathrm{G}}_{i}\mathbf{H}_k = \begin{bmatrix} \mathbf{0} & \cdots & {}^{\mathrm{G}}_{\mathrm{I}}\mathbf{H}_k & \cdots & \mathbf{0} & {}^{\mathrm{G}}_{\mathrm{G}}\mathbf{H}_k \end{bmatrix} \tag{20}$$

where the i^{th} block of ${}^{\mathrm{G}}_{i}\mathbf{H}_k$ is ${}^{\mathrm{G}}_{\mathrm{I}}\mathbf{H}_k$, the last block equals to ${}^{\mathrm{G}}_{\mathrm{G}}\mathbf{H}_k$, and all the others are $\mathbf{0}$. As a reminder, ${}^{\mathrm{G}}_{\mathrm{I}}\mathbf{H}_k$ and ${}^{\mathrm{G}}_{\mathrm{G}}\mathbf{H}_k$ are given in (6). It is also noteworthy that the lever arms between each IMU and the GNSS antenna should be accurately compensated during the filter update stage [15].

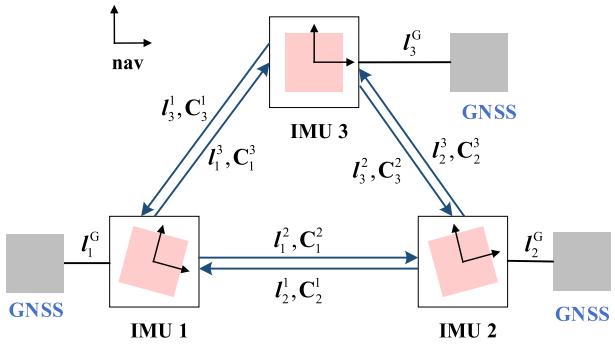

$\boldsymbol{l}^{\mathrm{G}}_{i}$ The lever arm between IMU i and GNSS antenna in the body frame of IMU i

Fig. 3. Illustration of the GNSS/MIMU integration architecture in the no-base form.

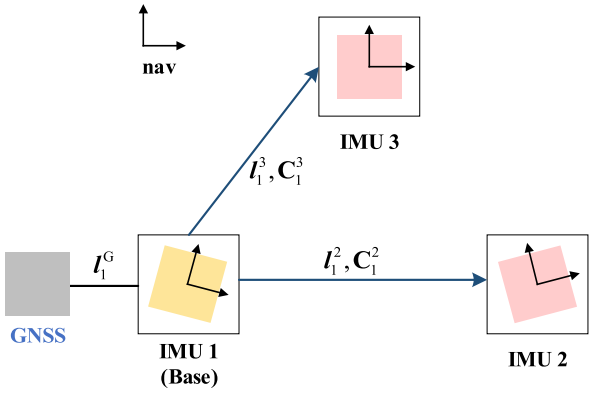

Fig. 4. Illustration of the GNSS/MIMU integration architecture in the base-centered form.

Finally, the measurement error covariance matrix is given by:

$$\mathbf{R}_k = blkdiag\left(\begin{bmatrix} \mathbf{0} & & \\ & \ddots & \\ & & \mathbf{0} \end{bmatrix}, \begin{bmatrix} {}^{\mathrm{G}}\mathbf{R}_k & \cdots & {}^{\mathrm{G}}\mathbf{R}_k \\ \vdots & \ddots & \vdots \\ {}^{\mathrm{G}}\mathbf{R}_k & \cdots & {}^{\mathrm{G}}\mathbf{R}_k \end{bmatrix}\right) \tag{21}$$

where $blkdiag()$ forms a block-diagonal matrix with the inside matrices.

2.2.2. Base-centered form

The measurement model in (19) contains much repetitive information. Therefore, we can use a smaller measurement model than (19) to completely describe all the effective information. This can be achieved by using the base-centered form to construct the measurement model. In this form, an arbitrary IMU is selected as the "base" (denoted by b), and we only use the relative pose information between the base and every other IMU. Besides, there is no need to clone the GNSS measurements. Fig. 4 illustrates the GNSS/MIMU integration architecture in the base-centered form.

In a general case, the measurement model is written as:

$$\begin{bmatrix} {}^{b}_{1}\mathbf{z}_k \\ \vdots \\ {}^{b}_{m}\mathbf{z}_k \\ {}^{\mathrm{G}}_{b}\mathbf{z}_k \end{bmatrix} = \begin{bmatrix} {}^{b}_{1}\mathbf{H}_k \\ \vdots \\ {}^{b}_{m}\mathbf{H}_k \\ {}^{\mathrm{G}}_{b}\mathbf{H}_k \end{bmatrix} \mathbf{x}_k + \begin{bmatrix} \mathbf{0} \\ \vdots \\ \mathbf{0} \\ {}^{\mathrm{G}}\boldsymbol{\upsilon}_k \end{bmatrix} \Longleftrightarrow \mathbf{z}_k = \mathbf{H}_k\mathbf{x}_k + \boldsymbol{\upsilon}_k \tag{22}$$

Note that ${}^{b}_{b}\mathbf{z}_k$ and ${}^{b}_{b}\mathbf{H}_k$ do not appear in this equation. Finally, the measurement error covariance matrix is given by:

$$\mathbf{R}_k = blkdiag\left(\begin{bmatrix}\mathbf{0} & & \\ & \ddots & \\ & & \mathbf{0}\end{bmatrix}, {}^{\mathrm{G}}\mathbf{R}_k\right) \tag{23}$$

2.2.3. Comments on the two forms

The no-based form and the base-centered one have their own advantages and disadvantages. On one hand, the measurement model in the no-base form contains much repetitive information, which will lead to a waste of computation and storage. Therefore, the base-centered form is preferred to the no-base one in practical applications. On the other hand, the no-base form offers straightforward proof of integrity in special cases, which will be shown in detail in Section 3.

Finally, it is worth noting that these two forms will generate the same navigation solutions because they both use all available information. For the same reason, the navigation outputs will not be influenced by the selection of the base. Besides, under the rigid-body assumption, the posterior (i.e., updated) position estimates corresponding to each IMU are consistent after calibrating the extrinsic parameters.

2.3. The advantages of the proposed GNSS/MIMU integration scheme

It is noteworthy that the approach above is not the only way to integrate multiple IMUs with GNSS. The integration can also be implemented based on the following two two-step schemes. In the first scheme, a consistency check for redundant IMUs is performed first, e.g., [37], and then GNSS is integrated with one of the IMUs. In the other scheme, the first step is to map the measurements from all IMUs onto a virtual IMU [38], and the second step is to integrate this IMU is integrated with GNSS.

Compared to these two-step schemes, the proposed approach mainly has three advantages, all of which benefit from the fact that the measurements from GNSS and all IMUs are fused in a centralized filter in this approach. First, the proposed approach facilitates the design of the integrity monitoring algorithm. To be more specific, this approach enables not only a capability of detecting GNSS faults and IMU failures simultaneously but also a straightforward evaluation of the corresponding protection levels. In contrast, for the two-step schemes above, it is not easy to develop the associated integrity monitoring methods. To the best of our knowledge, there is not yet a complete integrity monitoring approach for them. This is mainly because it requires complicated derivations to determine the detection thresholds against IMU faults and to quantify the effect of undetected IMU faults on the final protection levels.

Second, this approach fully exploits the measurements and the information redundancy provided by all sensors, and thus it can achieve better navigation accuracy and higher navigation integrity than other schemes. Conversely, in the two-step schemes above, there is either a waste of effective information or a waste of information redundancy. Third, it is conducive to the design of fault exclusion functions, which will be investigated in the future. Specifically, in this approach, the exclusion of IMU faults and GNSS faults can be straightforwardly implemented, even if the system includes only one or two IMUs.

3. Integrity monitoring for GNSS/MIMU tight integration

In this section, we propose an integrity monitoring scheme for the GNSS/MIMU tightly coupled system based on MHSS. This scheme includes three key steps: (a) determining the fault modes that need to be monitored, (b) constructing the test statistics and thresholds for fault detection, and (c) evaluating the protection levels. In the following, we first introduce the input parameters and then describe the three steps with detailed derivations.

Table 1
Parameters about the noise characteristics of IMU and GNSS measurements.

Sensor	Parameter	Description
IMU	${}^{\mathrm{I}}_{i}\sigma_{\mathrm{a},*}$, ${}^{\mathrm{I}}_{i}\sigma_{\mathrm{g},*}$	The STandard Deviations (STDs) of accelerometer and gyro white noises for IMU i. The subscript "$*$" indicates the body axis, i.e., $*= x, y, z$
	${}^{\mathrm{I}}_{i}\sigma_{\mathrm{ba},*}$, ${}^{\mathrm{I}}_{i}\sigma_{\mathrm{bg},*}$	The Gauss-Markov driving noise STDs of accelerometer and gyro biases
	${}^{\mathrm{I}}_{i}\tau_{\mathrm{ba},*}$, ${}^{\mathrm{I}}_{i}\tau_{\mathrm{bg},*}$	The Gauss-Markov process correlation time of accelerometer and gyro biases
GNSS	${}^{\mathrm{G}}\sigma_{\rho,i}$	The pseudorange error STD for Space Vehicle (SV, i.e., satellite) i
	${}^{\mathrm{G}}\sigma_{\mathrm{bias}}$	The white noise STD of the receiver clock bias
	${}^{\mathrm{G}}\sigma_{\mathrm{dft}}$	The Gauss-Markov process noise STD of the receiver clock drift
	${}^{\mathrm{G}}\tau_{\mathrm{dft}}$	The Gauss-Markov process correlation time of the receiver clock drift

Table 2
Parameters in the integrity support message for GNSS/MIMU tight integration.

Category	Parameter	Description
Noise	$\mathbf{P}_0$	Initial state error covariance
	${}^{\mathrm{I}}\mathbf{Q}$, ${}^{\mathrm{G}}\mathbf{Q}$	Process noise covariances for MIMU and GNSS, respectively
	${}^{\mathrm{G}}\mathbf{R}$	GNSS pseudorange noise covariance
Fault	$p_{\mathrm{sat},i}$	Prior fault probability of SV i
	$p_{\mathrm{const},i}$	Prior fault probability of constellation i
	$p_{\mathrm{imu},i}$	Prior fault probability of IMU i

3.1. Input parameters

The proposed integrity monitoring scheme requires three categories of input parameters: Table 1 gives the parameters that describe the noise characteristics of each sensor, Table 2 shows the Integrity Support Message (ISM), and Table 3 lists the navigation performance requirements. It is assumed that the parameters in Table 1 are completely accurate. In this case, the noise covariances in the ISM can be directly computed using these parameters. Besides, the initial state error is assumed to follow a zero-mean multi-dimensional normal distribution whose covariance is $\mathbf{P}_0$. Under these two assumptions, the indicated state error covariance $\hat{\mathbf{P}}_k$ from the filter is consistent with the actual estimation error characteristics, which is an important precondition for integrity evaluation.

The ISM also includes the prior fault probabilities of each satellite, constellation, and IMU. Note that a constellation fault is said to occur when multiple satellites in it are simultaneously faulted due to a common cause. These probabilities are usually obtained by analyzing long-term historical data such as the ephemerides from a satellite or the raw measurements from an IMU. Finally, please note that those GNSS faults caused by heavy multipath or non-line-of-sight interference are not considered in this work. This is justified because, first, UAM vehicles usually fly in the airspace above the city, and they generally take off or land in open-sky areas. Besides, these faults can be avoided by properly setting the receiver elevation mask angle.

3.2. Determination of the monitored fault modes

MHSS-based integrity monitoring methods require to run multiple filters in parallel, one for each monitored fault mode. A fault

Table 3
Parameters about navigation performance requirements.

Category	Parameter	Description
Integrity	P_{HMI}	Total integrity budget
	$P_{\mathrm{HMI},q}$	Integrity budget for the q^{th} position component; q=1, 2, 3 represents east, north, and up, respectively.
	P_{THRES}	Threshold for the integrity risk coming from unmonitored fault modes
Continuity	P_{FA}	Total continuity budget for false alarm
	$P_{\mathrm{FA},q}$	False alarm probability allocated to the q^{th} position component

mode is a hypothesis about the health status of each measurement. Each fault mode s is associated with three terms: (a) P_s-the prior probability of this hypothesis being true, (b) $\mathbb{S}_s$-a subset which includes the healthy measurements under this hypothesis, and (c) F_s-a filter that uses the measurements included in $\mathbb{S}_s$. s=0 corresponds to the hypothesis that the system is fault-free. Accordingly, F_0 is called "main filter" and the others are called "subfilters".

For a GNSS/MIMU tightly coupled system, a fault mode hypothesizes the health status of each visible SV and each IMU. Because a satellite or an IMU is either healthy or faulted, there will be 2^{m+n} collectively exclusive fault modes in total if the navigation system employs m IMUs and observes n satellites. In practice, it is not necessary to monitor all these fault modes, because the probability of most fault modes is significantly low.

There have been various methods to determine the fault modes that need monitoring [9,39,40], and the method given in the baseline ARAIM algorithm is used here [9]. The objective of this method is to find a list of fault modes, i.e., {0, 1, 2, ..., N_{S}}, such that

$$P_{\mathrm{NM}} = 1 - \sum_{s=0}^{N_{\mathrm{S}}} P_s \leq P_{\mathrm{THRES}} \tag{24}$$

where P_{NM} denotes the sum of the probabilities of every unmonitored fault mode. A detailed description of this method can be found in [9], and it is not presented here for the sake of brevity.

Although this method is originally developed for GNSS-standalone systems, it can be applied to GNSS/MIMU tightly integrated navigation systems after the following two modifications are made. First, each IMU is viewed as a virtual satellite, and the prior fault probability of this satellite is the same as that of the original IMU. Second, these virtual satellites are considered to form a virtual constellation whose prior fault probability is 0. To offer a clearer illustration of this method, Fig. 5 presents several examples of the fault modes for a GNSS/MIMU integrated system.

3.3. Construction of test statistics and thresholds for fault detection

Fault detection aims at timely detecting the faults in the system, which is a key function in integrity monitoring schemes. In this work, the FD function is implemented based on MHSS, and the corresponding test statistics and thresholds are determined as follows. For each fault mode $s > 0$, the test statistics are constructed based on the difference between the all-in-view solution from the main filter F_0 and the fault-tolerant solution from the subfilter F_s. F_s excludes the measurements that are hypothesized as faulted in this fault mode. For a clear view, Table 4 summarizes the rules for the exclusion of measurements for different fault modes.

As shown in Table 4, the rule is relatively complicated for the fault modes that hypothesize the base IMU to be faulted. This is because a new base IMU must be selected in this case. Therefore, we divide all the monitored fault modes into two groups: (a) G_1-the group of the fault modes that hypothesize the base IMU to be healthy and (b) G_2-the group of the rest fault modes. The determination of the test statistics and thresholds for these two groups of fault modes is presented as follows.

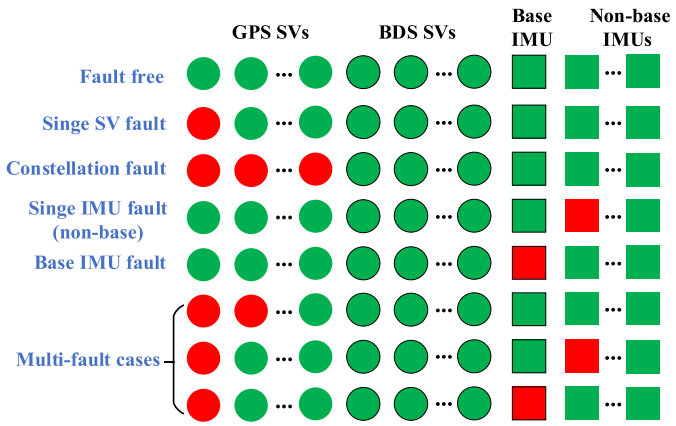

Fig. 5. Examples of different fault modes, where green indicates healthy and red means faulted. (For interpretation of the colors in the figure(s), the reader is referred to the web version of this article.)

For a fault mode $s \in \mathrm{G}_1$, the test statistics are computed by:

$$\boldsymbol{\Delta}\hat{\mathbf{p}}^{(s)} = {}^{\mathrm{I}}_{b}\hat{\mathbf{p}}^{(s)} - {}^{\mathrm{I}}_{b}\hat{\mathbf{p}}^{(0)} \tag{25}$$

where ${}^{\mathrm{I}}_{b}\hat{\mathbf{p}}^{(s)}$ and ${}^{\mathrm{I}}_{b}\hat{\mathbf{p}}^{(0)}$ are the position estimates of the base IMU given by F_s and F_0, respectively. Both of them are given in the local ENU frame, and thus the three elements of $\boldsymbol{\Delta}\hat{\mathbf{p}}^{(s)}$ are the test statistics in the east, north, and up directions in turn. Note that the subscript k is omitted hereafter for simplicity.

Then the covariance of the test statistics above is given by:

$$\boldsymbol{\Omega}^{(s)}_{\mathrm{ss}} \triangleq \mathbf{cov}\left(\boldsymbol{\Delta}\hat{\mathbf{p}}^{(s)}, \boldsymbol{\Delta}\hat{\mathbf{p}}^{(s)}\right) = {}^{\mathrm{I}}_{b}\hat{\mathbf{P}}^{(s)}_{\mathrm{p}} - {}^{\mathrm{I}}_{b}\hat{\mathbf{P}}^{(0)}_{\mathrm{p}} \tag{26}$$

where **cov** denotes the covariance of two vectors; ${}^{\mathrm{I}}_{b}\hat{\mathbf{P}}^{(s)}_{\mathrm{p}}$ and ${}^{\mathrm{I}}_{b}\hat{\mathbf{P}}^{(0)}_{\mathrm{p}}$ are the position error covariances output from F_s and F_0, respectively. The proof of this equation is given in Appendix B.

Let the index q=1, 2, and 3 designate the east, north, and up position components, respectively. For q from 1 to 3, the error variance of the q^{th} component of ${}^{\mathrm{I}}_{b}\hat{\mathbf{p}}^{(s)}$ is computed as:

$$\sigma^{(s)2}_{q} = \mathbf{e}_q^{\mathrm{T}} \cdot {}^{\mathrm{I}}_{b}\hat{\mathbf{P}}^{(s)}_{\mathrm{p}} \cdot \mathbf{e}_q \tag{27}$$

where $\mathbf{e}_q$ is a 3×1 vector whose q^{th} entry is 1 and all others are 0. Then, the test statistic for the q^{th} direction and its variance are respectively given by:

$$\Delta p^{(s)}_{q} = \mathbf{e}_q^{\mathrm{T}} \cdot \boldsymbol{\Delta}\hat{\mathbf{p}}^{(s)} \tag{28}$$

$$\sigma^{(s)2}_{\mathrm{ss},q} = \mathbf{e}_q^{\mathrm{T}} \cdot \boldsymbol{\Omega}^{(s)}_{\mathrm{ss}} \cdot \mathbf{e}_q \tag{29}$$

Based on (29), the threshold for the test statistic $\Delta p^{(s)}_{q}$ is determined by [9]:

$$T^{(s)}_{q} = \mathcal{Q}^{-1}\left(\frac{P_{\mathrm{FA},q}}{2N_{\mathrm{S}}}\right) \cdot \sigma^{(s)}_{\mathrm{ss},q} \tag{30}$$

where $\mathcal{Q}^{-1}(a)$ is the (1-a) quantile of a zero-mean unit-variance Gaussian distribution.

For a fault mode $s \in \mathrm{G}_2$, the determination of the test statistics and the thresholds will be more complicated than the procedures above. Because (22) gives the measurement model in a base-centered form, all the virtual measurements that are derived from MIMU relative pose information will be affected if the base IMU is faulted. Therefore, for $s \in \mathrm{G}_2$, we should select a new base $\acute{b}$ from the healthy IMUs. Accordingly, the measurement model in

Table 4
The rules for the exclusion of measurements for different fault modes.

Fault mode s	Example	Exclusion of measurements in F_s
Singe satellite fault	SV i is faulted	Remove the elements associated with this SV from ${}^{\mathrm{G}}_{b}\mathbf{z}_k$ in (22)
Single constellation fault	Constellation i is faulted	Remove the elements associated with this constellation from ${}^{\mathrm{G}}_{b}\mathbf{z}_k$ in (22)
Single non-base IMU fault	IMU i is faulted ($i \neq b$)	Remove ${}^{b}_{i}\mathbf{z}_k$ from $\mathbf{z}_k$ in (22)
Base IMU fault	IMU b is faulted	Select a new base IMU (denoted by $\acute{b}$), and then remove ${}^{\acute{b}}_{b}\mathbf{z}_k$ from the new $\mathbf{z}_k$ vector
Multi-fault cases	Multiple single-fault events occur simultaneously	Combine the operations above

(22) needs to be rewritten with the new base. In this case, the variance of the q^{th} component of ${}^{\mathrm{I}}_{\acute{b}}\hat{\mathbf{p}}^{(s)}$ is given by:

$$\sigma_q^{(s)2} = \mathbf{e}_q^{\mathrm{T}} \cdot {}^{\mathrm{I}}_{\acute{b}}\hat{\mathbf{P}}_{\mathrm{p}}^{(s)} \cdot \mathbf{e}_q \tag{31}$$

where ${}^{\mathrm{I}}_{\acute{b}}\hat{\mathbf{p}}^{(s)}$ and ${}^{\mathrm{I}}_{\acute{b}}\hat{\mathbf{P}}_{\mathrm{p}}^{(s)}$ are output from the new subfilter F_s.

Then the test statistics are computed as:

$$\boldsymbol{\Delta}\hat{\mathbf{p}}^{(s)} = \left({}^{\mathrm{I}}_{\acute{b}}\hat{\mathbf{p}}^{(s)} + \mathbf{C}_b^n \boldsymbol{l}_b^{\acute{b}}\right) - {}^{\mathrm{I}}_{b}\hat{\mathbf{p}}^{(0)} = {}^{\mathrm{I}}_{\acute{b}}\hat{\mathbf{p}}^{(s)} - {}^{\mathrm{I}}_{\acute{b}}\hat{\mathbf{p}}^{(0)} \tag{32}$$

where ${}^{\mathrm{I}}_{\acute{b}}\hat{\mathbf{p}}^{(0)}$ is given by the new main filter F_0. It is noteworthy that ${}^{\mathrm{I}}_{\acute{b}}\hat{\mathbf{p}}^{(0)}$ is exactly consistent with ${}^{\mathrm{I}}_{b}\hat{\mathbf{p}}^{(0)}$ after calibrating the extrinsic parameters. Thus, the covariance of the test statistics is written as:

$$\boldsymbol{\Omega}_{\mathrm{ss}}^{(s)} = {}^{\mathrm{I}}_{\acute{b}}\hat{\mathbf{P}}_{\mathrm{p}}^{(s)} - {}^{\mathrm{I}}_{\acute{b}}\hat{\mathbf{P}}_{\mathrm{p}}^{(0)} \tag{33}$$

Notice that ${}^{\mathrm{I}}_{\acute{b}}\hat{\mathbf{P}}_{\mathrm{p}}^{(0)}$ is equal to ${}^{\mathrm{I}}_{b}\hat{\mathbf{P}}_{\mathrm{p}}^{(0)}$. The proof of (33) is given in Appendix B. Finally, the test statistics and the thresholds, i.e., $\Delta p_q^{(s)}$ and $T_q^{(s)}$, can be determined based on (28)–(30).

A GNSS/MIMU tightly coupled system is declared to be healthy only if we have:

$$\tau_q = \max_s \left(\left| \Delta p_q^{(s)} \right| / T_q^{(s)} \right) < 1, \forall q \in [1, 2, 3] \tag{34}$$

where τ_q denotes the normalized test statistic. If any test fails, the fault detector will issue a fault alarm to the users. And if all tests pass, the protection levels can be calculated following the method in the next subsection.

3.4. Evaluation of the protection levels

The PL is a probabilistic error bound computed to guarantee that the probability of the absolute position error exceeding the said number is smaller than the allowable integrity risk. According to this definition, the PL for the qth position component is given by [9]:

$$P_{\mathrm{HMI},q} = \mathcal{P}\left(\mathbf{e}_q^{\mathrm{T}} \cdot \left| {}^{\mathrm{I}}_{b}\hat{\mathbf{p}}^{(0)} - {}^{I}_{b}\mathbf{p} \right| > PL_q, \text{ no fault alarm} \right) \tag{35}$$

where $\mathcal{P}(\blacksquare)$ denotes the probability of the event $\blacksquare$.

For MHSS-based integrity monitoring approaches, the PLs can be straightforwardly computed by solving the following equation [9]:

$$P_{\mathrm{HMI},q} - \frac{P_{\mathrm{HMI},q}}{P_{\mathrm{HMI}}} P_{\mathrm{NM}} = 2\mathcal{Q}\left(\frac{PL_q}{\sigma_q^{(0)}} \right) + \sum_{s=1}^{N_{\mathrm{S}}} \mathcal{Q}\left(\frac{PL_q - T_q^{(s)}}{\sigma_q^{(s)}} \right) \cdot P_s \tag{36}$$

where $\mathcal{Q}$ denotes the tail probability of a zero-mean unit-variance Gaussian distribution, and $\sigma_q^{(0)}$ is the fault-free positioning error STD for the qth component, i.e., $\sigma_q^{(0)2} = \mathbf{e}_q^{\mathrm{T}} \cdot {}^{\mathrm{I}}_{b}\hat{\mathbf{P}}_{\mathrm{p}}^{(0)} \cdot \mathbf{e}_q$. This equation can be solved using a half-interval search method, which is detailed in [9]. Finally, the VPL and HPL are respectively given by:

$$VPL = PL_3 \tag{37}$$

$$HPL = \sqrt{PL_1^2 + PL_2^2} \tag{38}$$

4. Performance evaluation

In this section, multiple sets of simulations are carried out to demonstrate the proposed method. Section 4.1 describes the simulation settings in detail. Then Section 4.2 evaluates the protection levels and verifies the fault detection capabilities under different scenarios. Finally, a sensitivity analysis is conducted in Section 4.3.

4.1. Simulation set-up

The simulations are carried out based on an example UAM operation scenario. The simulated trajectory is shown in Fig. 6, which is designed to represent an approaching phase of the vehicle. Table 5 lists the default simulation settings, and the ISM parameters in Table 2 can be determined based on the information here. Please note that a simple MIMU configuration is used in the default scenario, and the effect of MIMU configurations on navigation performance will be discussed in Section 4.3. The GNSS ephemeris is downloaded from https://cddis.nasa.gov/, which describes the satellite trajectories on July 1, 2021. Fig. 7 shows the skyplot of the visible satellites at the start epoch. Finally, Table 6 gives the values of navigation performance requirements. It is noteworthy that although these numbers are originally derived in civil aviation fields, they can also preliminarily represent the case in UAM scenarios.

4.2. Evaluation of protection levels and fault detection capabilities

Based on the simulation settings above, we evaluate the integrity performance of GNSS/MIMU tightly coupled systems in terms of PLs and FD capabilities. First, Fig. 8 compares the integrity performance of three different systems: (a) a GNSS/IMU tightly coupled system with a fault-free IMU, (b) a GNSS/IMU tightly coupled system with a probably-faulted IMU, and (c) a GNSS/MIMU tightly coupled system with three probably-faulted IMUs. The prior fault probability of each probably-faulted IMU is 10^{-5}.

The result suggests that for traditional GNSS/IMU tightly coupled systems, the PLs will dramatically increase when IMU faults need to be considered. This phenomenon was hardly reported in prior studies, while it does offer clear evidence that IMU faults can seriously degrade the integrity performance of a GNSS/IMU tightly coupled system. The theoretical explanation for this phenomenon is given as follows. For a fault mode that hypothesizes the only

Table 5
Default simulation settings for the GNSS/MIMU integrated navigation system.

Sensor	Parameter	Value
IMU (100 Hz)	Number of IMUs	3
	MIMU configuration	All IMUs have the same pose, and their noise characteristics and prior fault probabilities are also the same (see below)
	White noise (1σ)	G: 0.2 °/$\sqrt{\text{hr}}$ A: 120 μg/$\sqrt{\text{Hz}}$
	Time-correlated bias (1σ)	G: 2 °/hr A: 15 μg
	Correlation time	G: 1000 s A: 1000 s
	Initial constant bias (1σ)	G: 10 °/hr A: 200 μg
	Fault probability	10^{-5} /approach
GNSS (1 Hz)	Pseudorange noise (1σ)	1.0 m, white noise
	Constellation	GPS (G01-G32) and BDS-2 (C01-C14)
	Fault probability	satellite: 10^{-5} /approach; constellation: 10^{-5} /approach
	Ephemeris	BRDM00DLR_S_20211820000_01D_MN.rnx
	Start epoch (GPS Time)	00:00:00, 2021/07/01

Table 6
Values of the navigation performance requirements.

Parameter	Value (preliminary)
P_{HMI}	10^{-7}
$P_{\text{HMI},q}$	$P_{\text{HMI},1} = P_{\text{HMI},2} = 10^{-9}$; $P_{\text{HMI},3} = 9.8 \times 10^{-8}$
P_{THRES}	8×10^{-8}
P_{FA}	3.99×10^{-6}
$P_{\text{FA},q}$	$P_{\text{FA},1} = P_{\text{FA},2} = 4.5 \times 10^{-8}$; $P_{\text{FA},3} = 3.9 \times 10^{-6}$

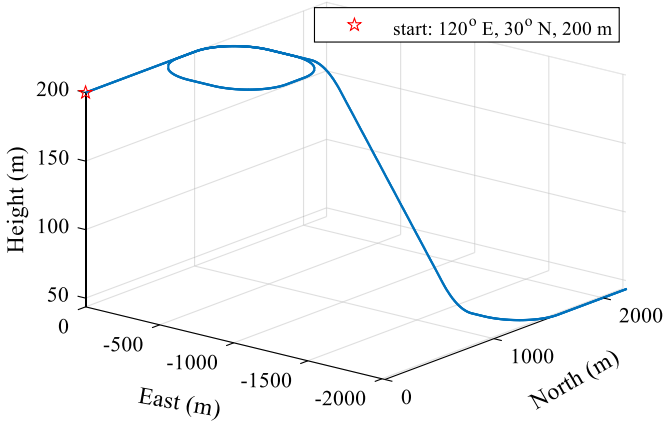

Fig. 6. The ground-truth flight trajectory.

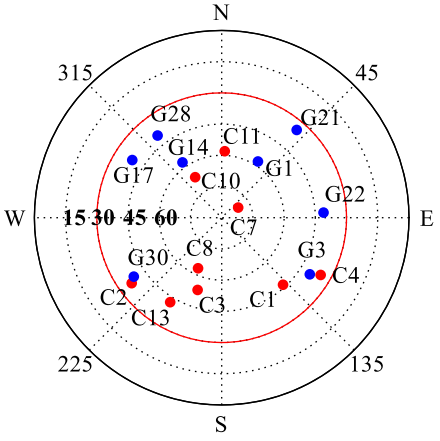

Fig. 7. Skyplot of the visible satellites at the start epoch.

IMU to be faulted, the corresponding subfilter degrades to a snapshot LS estimator that uses GNSS measurements only. Therefore, there will be a huge difference between the position estimates from this "subfilter" and the main filter, which results in large test thresholds for this fault mode. And according to (36), large test thresholds will significantly increase the PLs.

By comparing the PLs of systems (b) and (c) in Fig. 8, we can draw another conclusion: using multiple IMUs can effectively enhance navigation integrity when the prior probability of IMU faults is not negligible. Specifically, introducing redundant probably-faulted IMUs can significantly decrease the PLs and even make them lower than those of a GNSS/IMU tightly coupled system with a fault-free IMU. To conclude, this result highlights the importance of employing redundant IMUs for enhancing navigation integrity.

Then, the FD capability of the proposed integrity monitoring scheme is validated under the fault scenarios shown in Table 7. Fig. 9 demonstrates the behaviors of the fault detector in (a) a case of a single-satellite fault and (b) a case where two satellites are simultaneously faulted. Please note that in cases (a) and (b), the prior probabilities of satellite faults are set to 10^{-5} and 10^{-4}, respectively. This is because when the probability of satellite faults is 10^{-5}, there is no need to monitor the events of dual satellite faults. The top panel of this figure shows the normalized test statistics, τ, which are computed based on (34). And the bottom presents the normalized position errors, $|PE_q|/PL_q$, where PE_q denotes the position error in the q^{th} direction. It is noteworthy that in this figure and the following ones, the curves in the shaded area are meaningless because the navigation system will quit once a fault is detected. The results in this figure suggest the effectiveness of the proposed method in GNSS fault cases. To be more specific, this figure presents the following findings: (a) there is no false alarm when the system is fault-free; (b) the fault detector timely issues an alert when the system is threatened by GNSS faults; (c) the position errors are always bounded by (i.e., smaller than) the corresponding PLs when there is no alert.

Similarly, Fig. 10 and Fig. 11 show the fault detection results in the cases of an IMU ramp fault and an IMU step fault, respectively. The results indicate that the proposed integrity monitoring scheme can also protect the GNSS/MIMU tightly coupled system against IMU faults. Finally, Fig. 12 presents the fault detection result for a traditional GNSS/IMU tightly coupled system. And by comparing Fig. 10 and Fig. 12, it is clearly observed that employing redundant IMUs can not only improve the FD capability, i.e., shorten the time delay of alert, but also reduce the position errors caused by IMU faults.

4.3. Sensitivity analyses

The results above are obtained based on a simple MIMU configuration given in Table 5, while this subsection will discuss the sensitivity of navigation integrity over MIMU configurations. Three

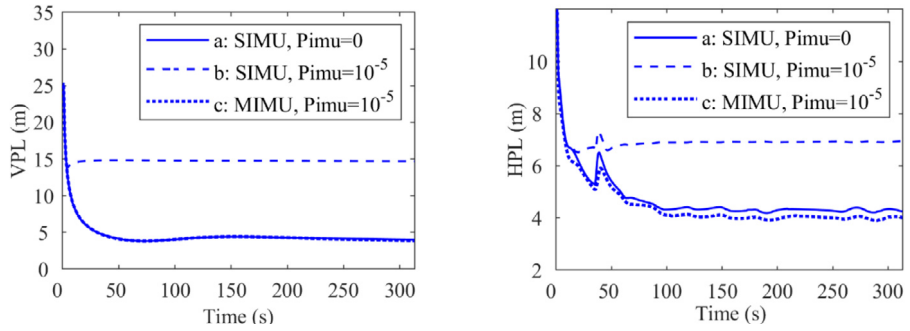

(a) VPL (b) HPL

Fig. 8. VPLs and HPLs of different systems, where "Pimu" denotes the prior probability of IMU faults and "SIMU" stands for "Single IMU".

Table 7
Simulation configurations in different cases.

Case	System	Fault source	Injected Fault(s)	Fault duration
Fig. 9a	GNSS/MIMU	GNSS	G21: ramp fault, 0.2 m/s	Since t=100 s
Fig. 9b			G21 & G22: ramp faults, 0.2 m/s	
Fig. 10		IMU	IMU 1, z-axis accelerometer: ramp fault, 0.01 m/s^3	
Fig. 11		IMU	IMU 1, z-axis accelerometer: step fault, 0.1 m/s^2	
Fig. 12	GNSS/IMU	IMU	z-axis accelerometer: ramp fault, 0.01 m/s^3	

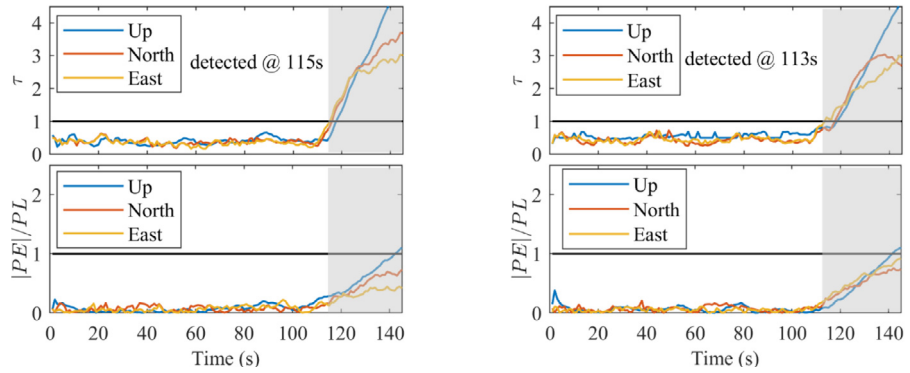

(a) singe satellite fault (b) dual satellite faults

Fig. 9. Fault detection results for the default GNSS/MIMU tightly coupled system in the presence of GNSS satellite faults.

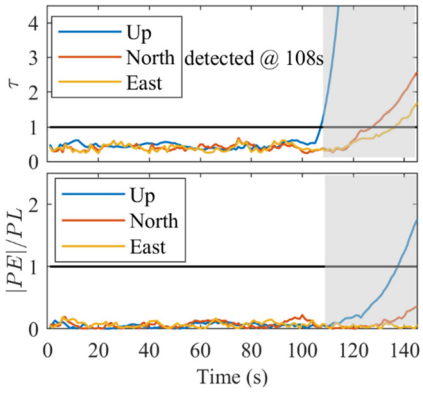

Fig. 10. Fault detection results for the default GNSS/MIMU tightly coupled system in the presence of an IMU ramp fault.

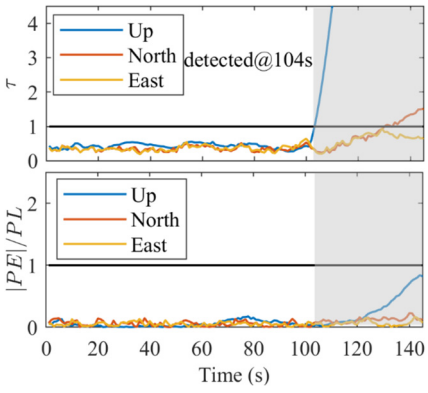

Fig. 11. Fault detection results for the default GNSS/MIMU tightly coupled system in the presence of an IMU step fault.

influencing factors are considered, including (a) the number of IMUs, (b) the IMU measurement accuracy, and (c) the installation geometry (i.e., extrinsic parameters) of the MIMU system.

First, Fig. 13 compares the PLs over different numbers of IMUs. The results reveal that increasing the number of IMUs can slightly improve the navigation integrity of GNSS/MIIMU tightly coupled systems. Besides, by comparing the PLs here with those of the

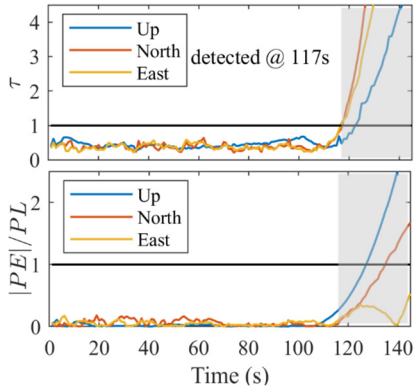

Fig. 12. Fault detection results for the traditional GNSS/IMU system in the presence of an IMU ramp fault.

standard GNSS/IMU system (see Fig. 8), we can observe that increasing the number of IMUs from 1 to 2 can provide more significant performance improvement than increasing it from 2 to 10. This is an interesting finding, and it can be interpreted as follows. Under the simulation condition given in Table 5, the probability of the event that all IMUs are simultaneously faulted is significantly low for a GNSS/MIMU system with 2 or more IMUs. Therefore, if the number of IMUs is equal to or higher than 2, there will be not any subfilter that degrades to a snapshot LS estimator. As explained before, this type of subfilter is the root cause of the dramatic increase in the PLs. Because increasing the number of IMUs from 1 to 2 can avoid running such subfilters, it can significantly reduce the PLs. On the other hand, increasing the number of IMUs from 2 to a higher value can improve the information redundancy, thereby slightly enhancing navigation integrity.

Then Fig. 14 reveals the effect of IMU measurement accuracy on the integrity performance. The error characteristics of the "normal" IMU are assumed to be the same as those given in Table 5. And the noise standard deviations of "good" and "bad" IMUs are respectively half and twice those of the "normal" IMU. It can be seen from Fig. 14 that IMU measurement accuracy is an important factor that influences the integrity performance of the GNSS/MIMU system. It is also observed that the integration of a "good" IMU and a "bad" one produces a similar performance to the system with two "good" IMUs. This may provide guidance for selecting the optimal MIMU configuration, which will be discussed in future work.

Finally, the effect of MIMU installation geometry on the integrity performance is investigated in Figs. 15 and 16. Without loss of generality, a GNSS/MIMU tightly coupled system with two IMUs is used as an example. The results indicate that MIMU installation geometry only has a subtle effect on the integrity performance, especially after the filter has converged. This finding implies that from the integrity perspective, there is no need to focus too much on designing the MIMU installation geometry.

5. Conclusions

In this work, we propose a method to enhance navigation integrity for Urban Air Mobility (UAM) by tightly integrating GNSS with redundant low-cost IMUs. The integration is realized based on a centralized Kalman filter, which fuses all measurements from each sensor and the virtual measurements derived from Multi-IMU (MIMU) relative pose information. Then an integrity monitoring scheme for the GNSS/MIMU tightly coupled system is developed based on multiple hypothesis solution separation. This scheme not only achieves real-time fault detection against all potential faults but also evaluates the corresponding protection levels. Simulation results suggest that (a) the integrity performance of traditional GNSS/IMU tightly coupled systems will be dramatically degraded if the probability of IMU failures is not negligible, and (b) employing redundant IMUs can greatly improve navigation integrity, i.e., lower the protection levels and enhance the fault detection capability. Sensitivity analysis results indicate that the integrity performance of GNSS/MIMU tightly coupled systems is mainly affected by IMU measurement accuracy and the number of IMUs, while it is not sensitive to relative poses among different IMUs. Future work will focus on designing an efficient fault exclusion algorithm for the proposed integrity monitoring scheme.

Declaration of competing interest

The authors declare that they have no known competing financial interests or personal relationships that could have appeared to influence the work reported in this paper.

Acknowledgements

This work was jointly supported by the National Key Research and Development Program of China (Grant Number: 2021YFB3901501) and the National Natural Science Foundation of China (Grant Numbers: 62103274 and 62173227). We would also like to thank Chao Qin from the University of Toronto, Canada, for the discussions on attitude representation methods.

Appendix A. Proof of Equations (16)–(18)

This appendix gives the proof of the measurement equations coming from the relative pose information between two IMUs. Recall that $\overline{n}_i$ and $\overline{n}_j$ represent the predicted navigation frames by the INS solutions of IMU i and IMU j, respectively. Then, (14) can be rewritten as:

$$\mathbf{C}_{\overline{n}_i}^{n}\mathbf{C}_{i}^{\overline{n}_i}\left(\mathbf{C}_{\overline{n}_j}^{n}\mathbf{C}_{j}^{\overline{n}_j}\mathbf{C}_{i}^{j}\right)^{-1}=\mathbf{I} \tag{39}$$

Then it further becomes:

$$\mathbf{C}_{\overline{n}_i}^{n}\mathbf{C}_{i}^{\overline{n}_i}\mathbf{C}_{j}^{i}\mathbf{C}_{\overline{n}_j}^{j}\mathbf{C}_{n}^{\overline{n}_j}=\mathbf{I} \tag{40}$$

Given that the difference between $\overline{n}_i$ and $\overline{n}_j$ is usually small, we have:

$$\mathbf{C}_{i}^{\overline{n}_i}\mathbf{C}_{j}^{i}\mathbf{C}_{\overline{n}_j}^{j}=\mathbf{C}_{\overline{n}_j}^{\overline{n}_i}\approx\mathbf{I}-\left({}_{j}^{i}\boldsymbol{\varphi}\right)^{\times} \tag{41}$$

Similarly, we have the following:

$$\mathbf{C}_{n}^{\overline{n}_i}\approx\mathbf{I}-\left({}_{i}^{\mathrm{I}}\delta\boldsymbol{\phi}\right)^{\times} \tag{42}$$

$$\mathbf{C}_{n}^{\overline{n}_j}\approx\mathbf{I}-\left({}_{j}^{\mathrm{I}}\delta\boldsymbol{\phi}\right)^{\times} \tag{43}$$

Substituting (41)–(43) into (40) yields:

$$\mathbf{I}+\left({}_{i}^{\mathrm{I}}\delta\boldsymbol{\phi}-{}_{j}^{i}\boldsymbol{\varphi}-{}_{j}^{\mathrm{I}}\delta\boldsymbol{\phi}\right)^{\times}\approx\mathbf{I} \tag{44}$$

And it further becomes:

$${}_{j}^{i}\boldsymbol{\varphi}\approx{}_{i}^{\mathrm{I}}\delta\boldsymbol{\phi}-{}_{j}^{\mathrm{I}}\delta\boldsymbol{\phi} \tag{45}$$

This forms the measurement equation derived from the relative-attitude information between IMU i and IMU j.

As for the relative-position information, it can be used as follows. (15) can be rewritten as:

$${}_{i}^{\mathrm{I}}\overline{\mathbf{p}}-{}_{i}^{\mathrm{I}}\delta\mathbf{p}-\left({}_{j}^{\mathrm{I}}\overline{\mathbf{p}}-{}_{j}^{\mathrm{I}}\delta\mathbf{p}+\mathbf{C}_{\overline{n}_i}^{n}\mathbf{C}_{i}^{\overline{n}_i}\boldsymbol{l}_{i}^{j}\right)=\mathbf{0} \tag{46}$$

Then we have:

$${}_{i}^{\mathrm{I}}\overline{\mathbf{p}}-{}_{j}^{\mathrm{I}}\overline{\mathbf{p}}={}_{i}^{\mathrm{I}}\delta\mathbf{p}-{}_{j}^{\mathrm{I}}\delta\mathbf{p}+\mathbf{C}_{\overline{n}_i}^{n}\mathbf{C}_{i}^{\overline{n}_i}\boldsymbol{l}_{i}^{j} \tag{47}$$

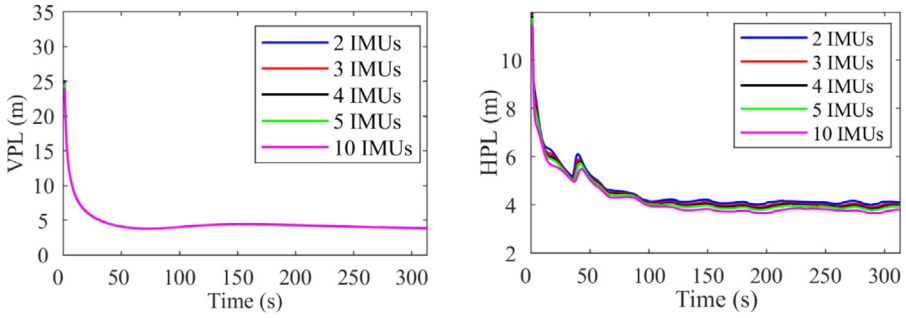

(a) VPL (b) HPL

Fig. 13. Comparison of the PLs over different numbers of IMUs.

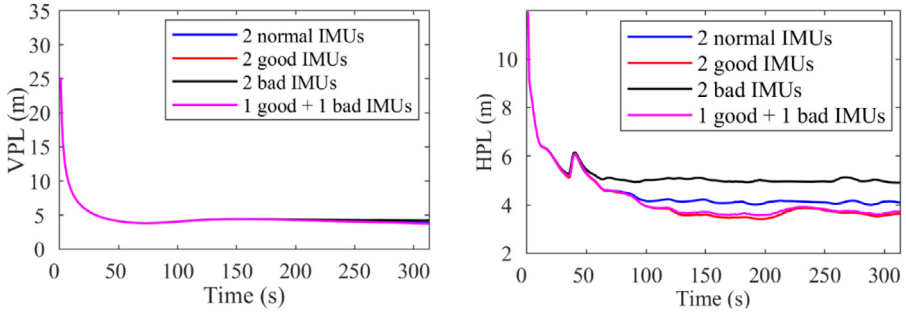

(a) VPL (b) HPL

Fig. 14. Sensitivity of the PLs over IMU measurement accuracy.

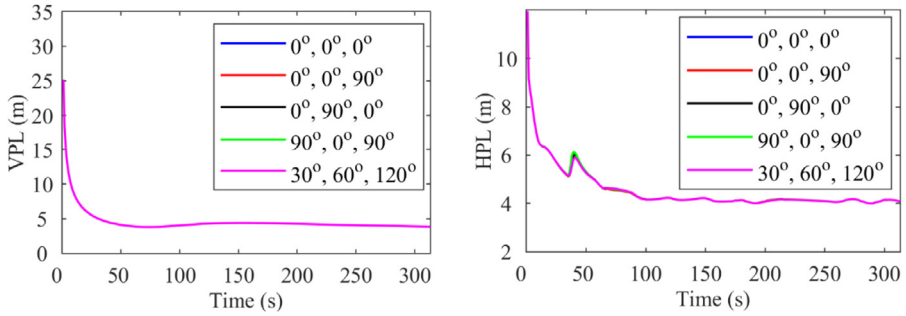

(a) VPL (b) HPL

Fig. 15. Comparison of the PLs over different dual-IMU relative attitudes, where the legend shows the Euler angles expressed in the body frame.

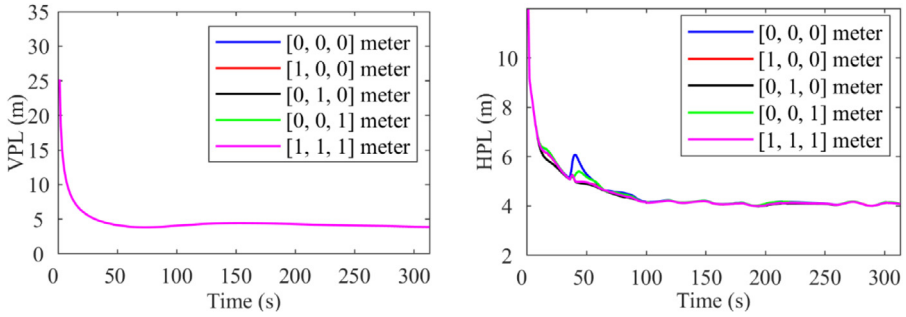

(a) VPL (b) HPL

Fig. 16. Comparison of the PLs over different dual-IMU relative positions, where the legend shows the relative position vector expressed in the body frame.

Substituting (42) into (47) yields:

$$ {}^{\mathrm{I}}_{i}\overline{\mathbf{p}} - {}^{\mathrm{I}}_{j}\overline{\mathbf{p}} - \mathbf{C}_i^{\overline{n}_i}\boldsymbol{l}_i^j = {}^{\mathrm{I}}_{i}\delta\mathbf{p} - {}^{\mathrm{I}}_{j}\delta\mathbf{p} + \left({}^{\mathrm{I}}_{i}\delta\boldsymbol{\phi}\right)^{\times}\cdot\mathbf{C}_i^{\overline{n}_i}\boldsymbol{l}_i^j \tag{48} $$

This forms the measurement equation derived from the relative-position information between IMU i and IMU j.

Rewriting (45) and (48) as a function of the state vector $\mathbf{x}$, we can obtain the measurement equation in a stack form:

$$ \mathbf{f}(\mathbf{x}) = \begin{bmatrix} {}^{\mathrm{I}}_{i}\delta\boldsymbol{\phi} - {}^{\mathrm{I}}_{j}\delta\boldsymbol{\phi} - {}^{i}_{j}\boldsymbol{\varphi} \\ {}^{\mathrm{I}}_{i}\delta\mathbf{p} - {}^{\mathrm{I}}_{j}\delta\mathbf{p} + \left({}^{\mathrm{I}}_{i}\delta\boldsymbol{\phi}\right)^{\times}\cdot\mathbf{C}_i^{\overline{n}_i}\boldsymbol{l}_i^j - \left({}^{\mathrm{I}}_{i}\overline{\mathbf{p}} - {}^{\mathrm{I}}_{j}\overline{\mathbf{p}} - \mathbf{C}_i^{\overline{n}_i}\boldsymbol{l}_i^j\right) \end{bmatrix} = \mathbf{0} \tag{49} $$

Finally, the corresponding measurement matrix given in (18) can be easily derived by taking the partial derivatives of $\mathbf{f}(\mathbf{x})$ over $\mathbf{x}$.

Appendix B. Proof of Equations (26) and (33)

In this appendix, the covariances of the solution separation test statistics for different fault modes are derived. First, the following lemma has been proved in [26], based on the results in [6] and the equivalence between a Kalman filter and a batch least-squares estimator.

Lemma 1. *Let* F *represent a Kalman filter and* $\mathrm{F}^{\mathrm{sub}}$ *denote one of its sub-filters. The measurement vector in* $\mathrm{F}^{\mathrm{sub}}$ *is a subset of that in* F. *For* F *and* $\mathrm{F}^{\mathrm{sub}}$, *we have:*

$$ \mathbf{cov}\left(\hat{\mathbf{X}}_k - \hat{\mathbf{X}}_k^{\mathrm{sub}}, \hat{\mathbf{X}}_k - \hat{\mathbf{X}}_k^{\mathrm{sub}}\right) = \hat{\mathbf{P}}_k - \hat{\mathbf{P}}_k^{\mathrm{sub}} \tag{50} $$

where $\hat{\mathbf{X}}_k$ *and* $\hat{\mathbf{X}}_k^{\mathrm{sub}}$ *are the state estimates output from* F *and* $\mathrm{F}^{\mathrm{sub}}$, *respectively;* $\hat{\mathbf{P}}_k$ *and* $\hat{\mathbf{P}}_k^{\mathrm{sub}}$ *are the corresponding error covariance matrices. Please note that this formula also applies to the error-state Kalman filter, and in that case,* $\mathbf{X}$ *represents the absolute state vector rather than the error state vector.*

Recall that (26) applies to each fault mode in G_1, for which the proof is given as follows. As a reminder, G_1 is the group of the monitored fault modes that hypothesize the base IMU is healthy. For a fault mode $s \in \mathrm{G}_1$, F_s is exactly a subfilter of the main filter F_0. Therefore, according to Lemma 1, (26) is valid in this case.

Besides, recall that (33) applies to each fault mode in G_2. And G_2 is the group of the monitored fault modes that assume the base IMU to be faulted. As illustrated in Section 2.2, the base-centered form is equivalent to the no-base form from the perspective of navigation results. Based on this equivalence, we have the following:

$$ {}^{\mathrm{I}}_{\acute{b}}\hat{\mathbf{p}}^{(0)} = \hat{\mathbf{p}}^{(0)}, {}^{\mathrm{I}}_{\acute{b}}\hat{\mathbf{P}}_{\mathrm{p}}^{(0)} = \hat{\mathbf{P}}_{\mathrm{p}}^{(0)} \tag{51} $$

where $\hat{\mathbf{p}}^{(0)}$ denotes the estimated position of IMU $\acute{b}$, and $\hat{\mathbf{P}}_{\mathrm{p}}^{(0)}$ is the associated error covariance. $\hat{\mathbf{p}}^{(0)}$ and $\hat{\mathbf{P}}_{\mathrm{p}}^{(0)}$ are both output from the main filter in the no-base form. In contrast, ${}^{\mathrm{I}}_{\acute{b}}\hat{\mathbf{p}}^{(0)}$ and ${}^{\mathrm{I}}_{\acute{b}}\hat{\mathbf{P}}_{\mathrm{p}}^{(0)}$ are obtained from the main filter in the base-centered form. After selecting a new base (i.e., IMU $\acute{b}$), each of the new subfilters in the base-centered form is still a subfilter of the main filter in the no-base form. Based on this conclusion and Lemma 1, we have the following:

$$ \mathbf{cov}\left({}^{\mathrm{I}}_{\acute{b}}\hat{\mathbf{p}}^{(s)} - {}^{\mathrm{I}}_{\acute{b}}\hat{\mathbf{p}}^{(0)}, {}^{\mathrm{I}}_{\acute{b}}\hat{\mathbf{p}}^{(s)} - {}^{\mathrm{I}}_{\acute{b}}\hat{\mathbf{p}}^{(0)}\right) = \mathbf{cov}\left({}^{\mathrm{I}}_{\acute{b}}\hat{\mathbf{p}}^{(s)} - \hat{\mathbf{p}}^{(0)}, {}^{\mathrm{I}}_{\acute{b}}\hat{\mathbf{p}}^{(s)} - \hat{\mathbf{p}}^{(0)}\right) \tag{52} $$

$$ \mathbf{cov}\left({}^{\mathrm{I}}_{\acute{b}}\hat{\mathbf{p}}^{(s)} - \hat{\mathbf{p}}^{(0)}, {}^{\mathrm{I}}_{\acute{b}}\hat{\mathbf{p}}^{(s)} - \hat{\mathbf{p}}^{(0)}\right) = {}^{\mathrm{I}}_{\acute{b}}\hat{\mathbf{P}}_{\mathrm{p}}^{(s)} - \hat{\mathbf{P}}_{\mathrm{p}}^{(0)} = {}^{\mathrm{I}}_{\acute{b}}\hat{\mathbf{P}}_{\mathrm{p}}^{(s)} - {}^{\mathrm{I}}_{\acute{b}}\hat{\mathbf{P}}_{\mathrm{p}}^{(0)} \tag{53} $$

This completes the proof of (33).

References

[1] W. Dai, B. Pang, K.H. Low, Conflict-free four-dimensional path planning for urban air mobility considering airspace occupancy, Aerosp. Sci. Technol. 119 (2021) 107154.
[2] M.D. Pavel, Understanding the control characteristics of electric vertical take-off and landing (eVTOL) aircraft for urban air mobility, Aerosp. Sci. Technol. 125 (2022) 107143.
[3] A. Mathur, K. Panesar, J. Kim, E.M. Atkins, N. Sarter, Paths to autonomous vehicle operations for urban air mobility, in: AIAA Aviation 2019 Forum, 2019, pp. 1–17.
[4] ICAO, Annex 10 - Aeronautical Telecommunications - Volume I - Radio Navigational Aids, Amendment 84, Montreal, QC, Canada, 2009.
[5] N. Zhu, J. Marais, D. Betaille, M. Berbineau, GNSS position integrity in urban environments: a review of literature, IEEE Trans. Intell. Transp. Syst. 19 (2018) 2762–2778.
[6] J. Blanch, T. Walter, P. Enge, RAIM with optimal integrity and continuity allocations under multiple failures, IEEE Trans. Aerosp. Electron. Syst. 46 (2010) 1235–1247.
[7] Q. Zeng, W. Qiu, J. Liu, R. Xu, J. Shi, Y. Sun, A high dynamics algorithm based on steepest ascent method for GNSS receiver, Chin. J. Aeronaut. 34 (2021) 177–186.
[8] R.G. Brown, A baseline GPS RAIM scheme and a note on the equivalence of three RAIM methods, J. Inst. Navig. 39 (1992) 301–316.
[9] J. Blanch, T. Walker, P. Enge, Y. Lee, B. Pervan, M. Rippl, A. Spletter, V. Kropp, Baseline advanced RAIM user algorithm and possible improvements, IEEE Trans. Aerosp. Electron. Syst. 51 (2015) 713–732.
[10] M. Joerger, B. Pervan, Fault detection and exclusion using solution separation and chi-squared ARAIM, IEEE Trans. Aerosp. Electron. Syst. 52 (2016) 726–742.
[11] Y. Zhai, M. Joerger, B. Pervan, Fault exclusion in multi-constellation global navigation satellite systems, J. Navig. 71 (2018) 1281–1298.
[12] Q. Meng, J. Liu, Q. Zeng, S. Feng, R. Xu, Impact of one satellite outage on ARAIM depleted constellation configurations, Chin. J. Aeronaut. 32 (2019) 967–977.
[13] W. Liu, M. Gu, M. Mou, Y. Hu, S. Wang, A distributed GNSS/INS integrated navigation system in a weak signal environment, Meas. Sci. Technol. 32 (2021) 115108.
[14] G. Zhang, L.T. Hsu, Intelligent GNSS/INS integrated navigation system for a commercial UAV flight control system, Aerosp. Sci. Technol. 80 (2018) 368–380.
[15] P. Groves, Principles of GNSS, Inertial and Multi-Sensor Integrated Navigation Systems, 2nd edition, Artech House, London, 2013.
[16] Y. Liang, Y. Jia, A nonlinear quaternion-based fault-tolerant SINS/GNSS integrated navigation method for autonomous UAVs, Aerosp. Sci. Technol. 40 (2015) 191–199.
[17] U.I. Bhatti, W.Y. Ochieng, S. Feng, Performance of rate detector algorithms for an integrated GPS/INS system in the presence of slowly growing error, GPS Solut. 16 (2012) 293–301.
[18] L. Zhong, J. Liu, R. Li, R. Wang, Approach for detecting soft faults in GPS/INS integrated navigation based on LS-SVM and AIME, J. Navig. 70 (2017) 561–579.
[19] S. Wang, X. Zhan, W. Pan, GNSS/INS tightly coupling system integrity monitoring by robust estimation, J. Aeronaut. Astronaut. Aviat. 50 (2018) 61–79.
[20] L. Yang, Y. Li, Y. Wu, C. Rizos, An enhanced MEMS-INS/GNSS integrated system with fault detection and exclusion capability for land vehicle navigation in urban areas, GPS Solut. 18 (2014) 593–603.
[21] C. Tanil, S. Khanafseh, M. Joerger, B. Pervan, Sequential integrity monitoring for Kalman filter innovations-based detectors, in: Proceedings of the 31st International Technical Meeting of the Satellite Division of The Institute of Navigation (ION GNSS+ 2018), 2018, pp. 2440–2455.
[22] G.D. Arana, O.A. Hafez, M. Joerger, M. Spenko, Recursive integrity monitoring for mobile robot localization safety, in: International Conference on Robotics and Automation 2019, 2019, pp. 305–311.
[23] O.G. Crespillo, A. Grosch, J. Skaloud, M. Meurer, Innovation vs residual KF based GNSS/INS autonomous integrity monitoring in single fault scenario, in: Proceedings of the 30th International Technical Meeting of the Satellite Division of The Institute of Navigation (ION GNSS+ 2017), 2018, pp. 2126–2136.
[24] M. Joerger, B. Pervan, Kalman filter-based integrity monitoring against sensor faults, J. Guid. Control Dyn. 36 (2013) 349–361.
[25] E.U.-U.S. Cooperation on Satellite Navigation Working Group C, ARAIM technical subgroup milestone 3 report, 2016.
[26] K. Gunning, J. Blanch, T. Walter, L. de Groot, L. Norman, Design and evaluation of integrity algorithms for PPP in kinematic applications, in: Proceedings of the 31st International Technical Meeting of the Satellite Division of The Institute of Navigation (ION GNSS+ 2018), 2018, pp. 1910–1939.
[27] C. Tanil, S. Khanafseh, M. Joerger, B. Kujur, B. Kruger, L. De Groot, B. Pervan, Optimal INS/GNSS coupling for autonomous car positioning integrity, in: Proceedings of the 32nd International Technical Meeting of the Satellite Division of The Institute of Navigation (ION GNSS+ 2019), 2019, pp. 3123–3140.
[28] S. Wang, X. Zhan, Y. Zhai, C. Chi, X. Liu, Ensuring high navigation integrity for urban air mobility using tightly coupled GNSS/INS system, J. Aeronaut. Astronaut. Aviat. 52 (2020) 429–442.
[29] Q. Meng, L.T. Hsu, Integrity monitoring for all-source navigation enhanced by Kalman filter based solution separation, IEEE Sens. J. 21 (2021) 15469–15484.

[30] M. Crispoltoni, M.L. Fravolini, F. Balzano, S. D'Urso, M.R. Napolitano, Interval fuzzy model for robust aircraft IMU sensors fault detection, Sensors 18 (2018) 2488.
[31] Sensonor, STIM 210 product brief, available at https://sensonor.azurewebsites.net/media/1042/product-brief-stim210.pdf. (Accessed 10 March 2022).
[32] Honeywell, Honeywell HG4930 product datasheet, available at https://media.digikey.com/pdf/Data%20Sheets/Honeywell%20PDFs/HG4930_PerfandEnvrioManual_Jul2017.pdf. (Accessed 10 March 2022).
[33] S. Wang, X. Zhan, Y. Zhai, B. Liu, Fault detection and exclusion for tightly coupled GNSS/INS system considering fault in state prediction, Sensors 20 (2020) 590.
[34] J. Lee, M. Kim, J. Lee, S. Pullen, Integrity assurance of Kalman-filter based GNSS/IMU integrated systems against IMU faults for UAV applications, in: Proceedings of the 31st International Technical Meeting of the Satellite Division of The Institute of Navigation (ION GNSS+ 2018), 2018, pp. 2484–2500.
[35] A. Angrisano, GNSS/INS integration methods, Ph.D. Dissertation, University of Calgary, 2010.
[36] K. Eckenhoff, P. Geneva, G. Huang, MIMC-VINS: a versatile and resilient multi-IMU multi-camera visual-inertial navigation system, IEEE Trans. Robot. 37 (2021) 1360–1380.
[37] S. Guerrier, A. Waegli, J. Skaloud, M.P. Victoria-Feser, Fault detection and isolation in multiple MEMS-IMUs configurations, IEEE Trans. Aerosp. Electron. Syst. 48 (2012) 2015–2031.
[38] M. Zhang, X. Xu, Y. Chen, M. Li, A lightweight and accurate localization algorithm using multiple inertial measurement units, IEEE Robot. Autom. Lett. 5 (2020) 1508–1515.
[39] Q. Meng, J. Liu, Q. Zeng, S. Feng, R. Xu, Improved ARAIM fault modes determination scheme based on feedback structure with probability accumulation, GPS Solut. 23 (2019) 1–11.
[40] Q. Meng, J. Liu, Q. Zeng, S. Feng, R. Xu, Reduced ARAIM subsets method determined by threshold for integrity risk, in: China Satellite Navigation Conference 2018 Proceedings Volume I, 2018, pp. 701–711.